


# Microstructure and Electrochemical Properties of $\text{ZnMn}_2\text{O}_4$ Nanopowder Synthesized Using Different Surfactants

XUELIANG ZHU,<sup>1,2</sup> ZHIQIANG WEI<sup>1,2,3</sup> , WENHUA ZHAO,<sup>2</sup>  
XUDONG ZHANG,<sup>2</sup> LI ZHANG,<sup>1,2</sup> and XUAN WANG<sup>1,2</sup>

1.—State Key Laboratory of Advanced Processing and Recycling of Non-ferrous Metals, Lanzhou University of Technology, Lanzhou 730050, China. 2.—School of Science, Lanzhou University of Technology, Lanzhou 730050, China. 3.—e-mail: qianweizuo@163.com

$\text{ZnMn}_2\text{O}_4$  (ZMO) nanopowders have been synthesized by a hydrothermal method using different surfactants [cetyltrimethylammonium bromide (CTAB), polyethylene glycol (PEG)-400, and Polysorbate-80]. The as-prepared  $\text{ZnMn}_2\text{O}_4$  samples exhibited single phase with tetragonal structure, showing honeycomb, spinel microsphere, and flower-cluster morphology, respectively. Cyclic voltammetry curves for all samples presented rectangular shape with symmetric nature and good cycling properties, with no obvious redox peak. Galvanostatic charge–discharge curves were triangular and symmetric. The specific capacitance of the  $\text{ZnMn}_2\text{O}_4$  nanopowders gradually decreased with increase of the scanning rate. ZMO-PEG exhibited higher specific capacitance of  $191 \text{ F g}^{-1}$  at scan rate of  $5 \text{ mV s}^{-1}$  and retained superior large-current cycling stability of 98.4% after 1000 cycles compared with ZMO-CTAB (93.8%) or ZMO-Polysorbate-80 (97.7%). Electrochemical impedance spectroscopy revealed that the  $\text{ZnMn}_2\text{O}_4$  nanopowders had low resistance. These results suggest that  $\text{ZnMn}_2\text{O}_4$  nanopowders have good capacitance characteristics.

**Key words:**  $\text{ZnMn}_2\text{O}_4$ , supercapacitors, surfactants, morphology, electrochemical properties

## INTRODUCTION

Over recent years, spinel-structured mixed transition-metal oxides<sup>1,2</sup> have aroused intense research interest due to their novel properties and broad application prospects in different areas such as biomedicine, ceramics, catalysis, electrode materials,<sup>3,4</sup> photoelectric conversion, magnetic resonance imaging,<sup>5</sup> photocatalysis, gas sensing,<sup>6,7</sup> etc. Spinel-structured mixed metal oxides ideally have the formula  $\text{AB}_2\text{O}_4$ , where A denotes the divalent metal ions occupying tetrahedral sites and B represents the trivalent metal ions occupying octahedral sites of the cubic crystal structure.<sup>8,9</sup> Nanoscale  $\text{ZnMn}_2\text{O}_4$  is a direct wide-bandgap semiconductor material with low bandgap energy (1.86 eV), belonging to space group  $I41/amd$ .<sup>10,11</sup> The microstructure

and band structure of nanomaterials primarily depend on the synthesis method applied as well as the processing conditions.<sup>12,13</sup> The crystal structure and band structure of  $\text{ZnMn}_2\text{O}_4$  nanocrystals can be modified by controlling the preparation process and changing the surfactant used, further improving their magnetic and optical properties.<sup>14,15</sup>  $\text{ZnMn}_2\text{O}_4$  has been studied as an anode material for lithium-ion batteries, having theoretical specific capacity of  $1025 \text{ mAh g}^{-1}$ .<sup>16,17</sup> However, there are few reports about  $\text{ZnMn}_2\text{O}_4$  supercapacitors.

To date, spinel-structured  $\text{ZnMn}_2\text{O}_4$  has been synthesized using various methods, for example, coprecipitation,<sup>18</sup> sonochemical emulsification,<sup>19</sup> hydrothermal method,<sup>20</sup> solid-state reaction (SSR),<sup>21</sup> sol–gel method,<sup>22</sup> etc. Among these, the hydrothermal method is a versatile technique for preparation of nanocrystalline powders due to its unique features such as production of well-crystalline, pure, and chemically homogeneous

nanopowders at low temperature. The solvent interacts with the reactants at molecular level, providing easy control of composition and structure, better control of stoichiometry, and the ability to tailor the particle size and morphology. For electrode materials, researchers have studied how to change the microscopic structure of such materials to improve their electrochemical properties.

In this work, the effect of different surfactants on the crystal structure, band structure, microstructure, and optical properties of ZnMn<sub>2</sub>O<sub>4</sub> nanopowders synthesized by the hydrothermal method were characterized using x-ray diffraction (XRD) analysis, scanning electron microscopy (SEM), x-ray energy-dispersive spectroscopy (XEDS), and ultraviolet–visible (UV–Vis) spectroscopy. Cyclic voltammetry (CV), galvanostatic charge–discharge (GCD) measurements, and electrochemical impedance spectroscopy (EIS) were investigated to characterize the electrochemical performance of the composites as electrode materials for supercapacitors.

## EXPERIMENTAL PROCEDURES

### Materials Preparation

Analytical-grade reagents Zn(NO<sub>3</sub>)<sub>2</sub>, Mn(NO<sub>3</sub>)<sub>2</sub>, citric acid, cetyltrimethylammonium bromide (CTAB), polyethylene glycol (PEG)-400, Polysorbate-80, absolute ethyl alcohol, and deionized water were used in all experiments. All chemical reagents were used as received without further purification. Zn(NO<sub>3</sub>)<sub>2</sub> (2.25 mmol), 4.5 mmol Mn(NO<sub>3</sub>)<sub>2</sub>, and 2.25 mmol citric acid were dissolved in 50 mL absolute ethyl alcohol and 30 mL deionized water under vigorous magnetic stirring for 30 min. Subsequently, 0.25 mmol of each surfactant was added into the above solution. The mixture was magnetically stirred at room temperature for 5 h. Finally, the prepared solution was transferred into a 100-mL Teflon-lined stainless-steel autoclave, and heated at 160°C for 24 h in an oven, then cooled to room temperature naturally. Thereafter, the products were obtained by centrifuging, washing, and drying under vacuum at 60°C for 12 h. The resulting products, denoted as ZMO-CTAB, ZMO-PEG, and ZMO-Polysorbate, were collected and used for further studies.

### Characterization

After synthesis, phase identification of the prepared nanoparticles was conducted by powder x-ray diffractometry (Rigaku Corporation, D/max-2400, Tokyo, Japan) using Cu K<sub>α</sub> radiation ( $\lambda = 1.54178 \text{ \AA}$ ) in the  $2\theta$  scan range from 20° to 80°. The morphology, composition, and size of the nanoparticles were characterized by SEM (Quanta FEG 200) equipped with XEDS. The electronic absorption behavior of the samples was investigated using UV–Vis spectroscopy (TU-1901).

Their electrochemical performance was measured using an electrochemical workstation (CS350, Wuhan CorrTest, China) in Na<sub>2</sub>SO<sub>4</sub> (0.5 M) aqueous solution in a standard three-electrode setup with ZMO nanopowder as working electrode, Pt sheet as counterelectrode, and KCl-saturated solution as reference electrode. CV curves were recorded at room temperature between  $-0.1 \text{ V}$  and  $0.7 \text{ V}$  using various scan rates from  $5 \text{ mV s}^{-1}$  to  $100 \text{ mV s}^{-1}$ . EIS measurements were carried out with a superimposed 5-mV sinusoidal voltage in the frequency range from 100 kHz to 0.01 Hz. GCD curves were measured between  $0.25 \text{ A g}^{-1}$  and  $3.5 \text{ A g}^{-1}$ .

The specific capacitance  $C$  ( $\text{F g}^{-1}$ ) of a sample can be calculated as<sup>23</sup>

$$C = I\Delta t / M \cdot \Delta V, \quad (1)$$

where  $C$  is the specific capacitance ( $\text{F g}^{-1}$ ),  $I$  is the discharge current (A),  $\Delta t$  is the discharge time (s),  $\Delta V$  is the voltage interval (V), and  $M$  represent the mass of electroactive material (g).

## RESULTS AND DISCUSSION

### Structural Characterization

The XRD patterns of the ZnMn<sub>2</sub>O<sub>4</sub> samples synthesized using different surfactants (CTAB, PEG-400, and Polysorbate-80) are shown in Fig. 1. Clearly, all the diffraction peaks could be well indexed to the spinel ZnMn<sub>2</sub>O<sub>4</sub> tetragonal structure, matching well with the standard spectrum in Joint Committee on Powder Diffraction Standards (JCPDS) card no. 77-2499 in space group  $I41/amd$  with  $a = 0.5722 \text{ nm}$ ,  $b = 0.5722 \text{ nm}$ , and  $c = 0.9326 \text{ nm}$ . These peaks can be assigned to reflections from (112), (200), (103), (211), (220), (105), (312), (321), and (221) crystallographic planes, respectively. In addition, no extra diffraction peaks assignable to other impurities were

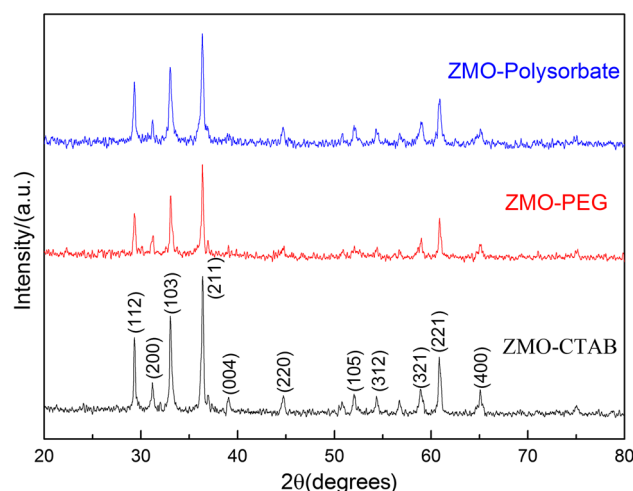
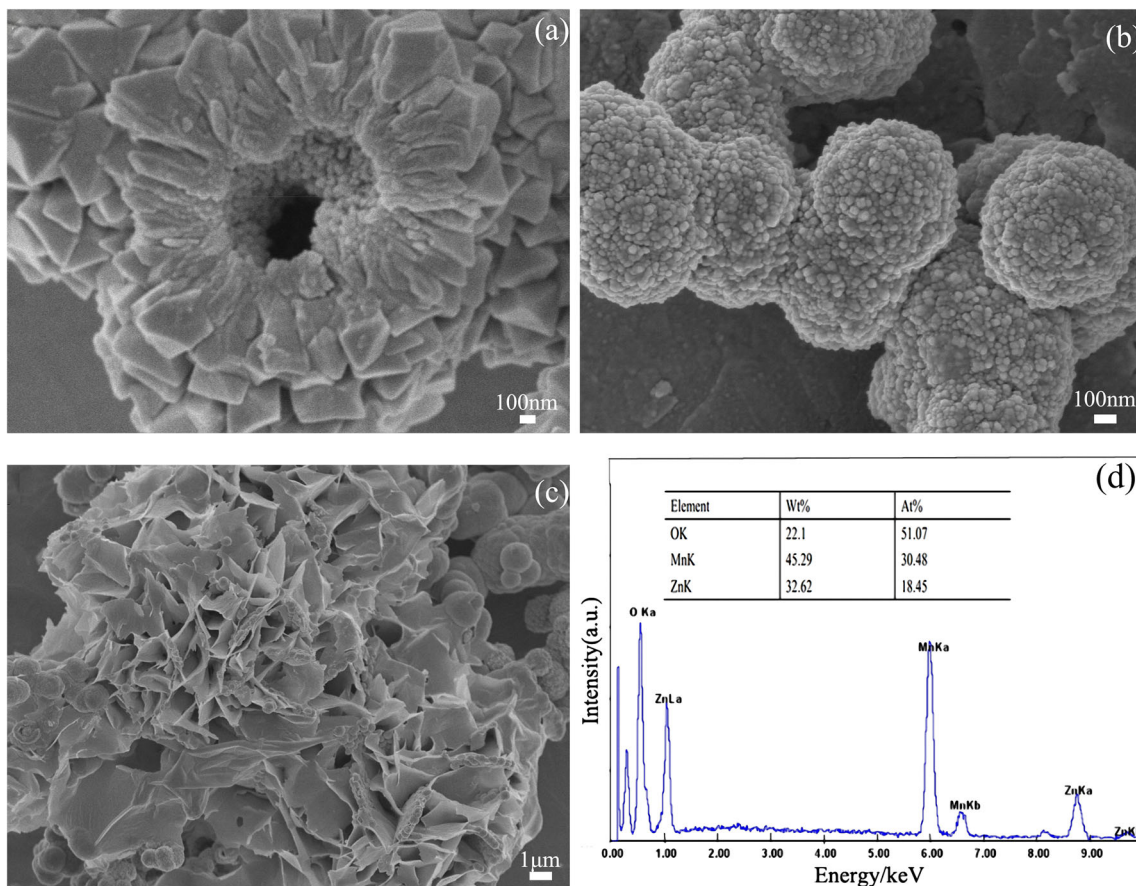


Fig. 1. XRD patterns of ZMO samples.

**Table I. XRD results for  $\text{ZnMn}_2\text{O}_4$  prepared using different surfactants**

Sample	$2\theta$ ( $^\circ$ )	FWHM ( $^\circ$ )	$d_{hkl}$ (nm)	$D$ (nm)	Lattice constants (nm)
ZMO-CTAB	36.379	0.157	0.2466	52.66	$a = 0.5725, c = 0.9226$
ZMO-PEG	36.373	0.144	0.2467	57.42	$a = 0.5732, c = 0.9203$
ZMO-Polysorbate	36.355	0.189	0.2469	43.75	$a = 0.5727, c = 0.9216$

**Fig. 2.** SEM images of (a) ZMO-CTAB, (b) ZMO-PEG, and (c) ZMO-Polysorbate samples. (d) XEDS spectrum of ZMO-PEG sample.

detected in the XRD patterns, showing that the as-synthesized samples consisted of a pure single phase.

The position of the most intense diffraction peak (211) was used in the Debye–Scherrer formula,  $D = \frac{K\lambda}{B \cos \theta}$ , where  $D$  represents the crystallite size,  $K = 0.89$  is the Scherrer constant,  $\theta$  is the Bragg diffraction angle, and  $B$  is the full-width at half-maximum (FWHM) of the (211) plane in radians. The calculated crystallite size for the samples is summarized in Table I, clearly being largest for the ZMO-PEG sample and smallest for the ZMO-Polysorbate sample. These results for the as-prepared samples synthesized using different surfactants suggest that the choice of surfactant indeed influences the crystallite size.

According to the Bragg formula,  $2d_{hkl} \sin \theta = \lambda$ , where  $d_{hkl}$  denotes the crystalline plane distance for

indices ( $hkl$ ) and  $\theta$  is the diffraction angle of the (211) peak, it can be understood that decrease of the crystal plane distance will lead to an increase of the diffraction angle. For tetragonal crystal structure,  $\frac{1}{d_{hkl}^2} = \frac{h^2 + k^2}{a^2} + \frac{l^2}{c^2}$ , where the lattice parameter ( $a$ ) can be calculated from measured values of the (211) plane spacing. The crystalline plane distance and lattice constant of the ZMO samples are presented in Table I. The changes in peak position, width, and intensity depend on the lattice parameter, which can mainly be attributed to the different structures of the  $\text{ZnMn}_2\text{O}_4$  samples depending on the choice of surfactant.

### Morphological Studies

SEM images of the ZMO samples are shown in Fig. 2. Particle agglomeration leads to the packed



structure observed in Fig. 2a. The ZMO-CTAB sample exhibited loose and coarse honeycomb-like morphology, ascribed to densely packed nanoparticles with distinct octahedral structure. A SEM image of the ZMO-PEG sample is shown in Fig. 2b, clearly revealing loose morphology with porous microsphere architecture composed of many nanoparticles; the average diameter of the rough and porous microspheres is about 500 nm. This structure contributes to improving the electrochemical performance. Figure 2c presents a SEM image of the ZMO-Polysorbate sample, showing loose and rough flower-like microsphere morphology composed of massive, irregular nanosheets. From the above observations, it is evident that the choice of surfactant has a great influence on the morphology and size of the resulting ZMO. In this work, the three different types of surfactant were added to absolute ethanol and deionized water as solvent. It is speculated that they were esterified with ethanol in the solvent then acted on metal ions of ZMO to form different states. Surfactants are mainly used to reduce the surface tension of ethanol and water in the solvent and to catalyze the reaction between ions. However, their reaction ability to polymerize ions in the solvent is different, as is the resulting microstructure: CTAB is an ionic surfactant that possesses many polar and nonpolar groups, showing good action for salt ions in water. CTAB shows general ability to polymerize solvent ions, resulting in a honeycomb structure with massive spinel-structure stacking. However, PEG and Polysorbate are nonionic polymeric surfactants. The C–H functional group on their polymer chain carries a considerable number of polar groups. As an alcohol, PEG has a much shorter hydrocarbon chain than Polysorbate, which is an ester, so its weaker ability to carry polar groups and catalyze solvent ions will cause ions in the solvent to form a compact nano/microsphere structure. Polysorbate has strong ability to polymerize solvent ions and will thus form a large nanosheet-like structure.

To further clarify the chemical components of the as-prepared samples, the XEDS spectrum of the ZMO-PEG sample is shown in Fig. 2d, clearly revealing that ZMO-PEG mainly exhibits peaks characteristic of Zn, Mn, and O elements. The characteristic peak at 0.5 keV is the O signal, while peaks characteristic of Zn appear at 1.0 keV and 8.8 keV, and those at 6.0 keV and 6.6 keV can be assigned to elemental Mn. The quantitative atomic and weight percentages of the compositional elements are shown in the inset to Fig. 2d, being nearly equal to the nominal stoichiometry within experimental error. These XEDS results further verify the conclusions based on the XRD analysis above, confirming that spinel  $\text{ZnMn}_2\text{O}_4$  nanopowders were successfully synthesized by the hydrothermal method using the different surfactants.

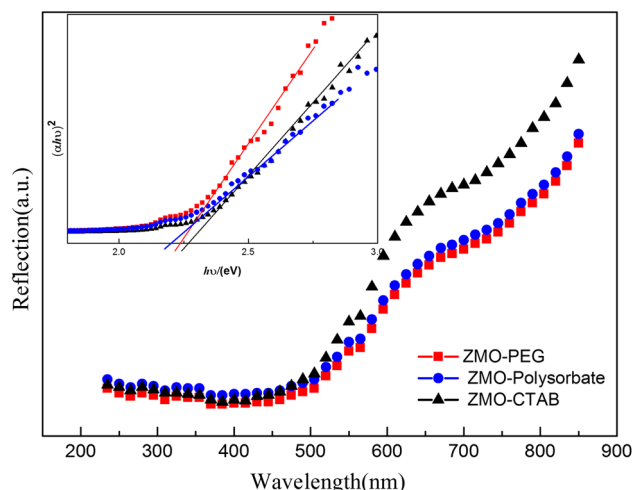


Fig. 3. Diffuse reflectance spectra and  $(\alpha h\nu)^2$  versus  $h\nu$  curves (inset) of ZMO samples.

### Optical Properties

To study the effect of the different surfactants on the optical characteristics of the resulting  $\text{ZnMn}_2\text{O}_4$  nanocrystals, UV–Vis diffuse reflectance spectroscopy (DRS) measurements were carried out (Fig. 3). For these  $\text{ZnMn}_2\text{O}_4$  samples with a direct band structure, the optical bandgap  $E_g$  can be approximated from optical reflectance data using the Tauc rule:  $[F(R)\alpha h\nu]^2 = A(h\nu - E_g)$ , where  $h\nu$  is the incident photon energy,  $\nu$  is the photon frequency,  $E_g$  is the optical bandgap, and  $A = 4\pi k/\lambda$  represents the absorption coefficient. The bandgap energy of the  $\text{ZnMn}_2\text{O}_4$  nanocrystals was estimated using the Kubelka–Munk function  $F(R) = (1 - R)^2/2R$  and the diffuse reflectance spectra by plotting  $(\alpha h\nu)^2$  versus  $h\nu$ . The  $E_g$  value for each sample was obtained by extrapolating the straight portion of the curve to the  $h\nu$  axis at  $\alpha = 0$ , as shown in the inset of Fig. 3. The resulting values of the optical bandgap energy for the ZMO-CTAB, ZMO-PEG, and ZMO-Polysorbate samples were 2.29 eV, 2.23 eV, and 2.18 eV, revealing that the different ZMO samples exhibited different bandgap values. This may be due to additional sub-bandgap energy levels induced by structural components, as well as abundant surface and interface defects in the agglomerated nanoparticles. Such change in the bandgap of the  $\text{ZnMn}_2\text{O}_4$  nanoparticles may also be associated with distortion of the lattice parameters due to quantum confinement effects arising from their small scale.

### Electrochemical Characterization

Figure 4a, b, and c show CV curves of the ZMO-CTAB, ZMO-PEG, and ZMO-Polysorbate electrodes obtained at various scan rates from  $5 \text{ mV s}^{-1}$  to  $100 \text{ mV s}^{-1}$ . It can be seen that all the samples

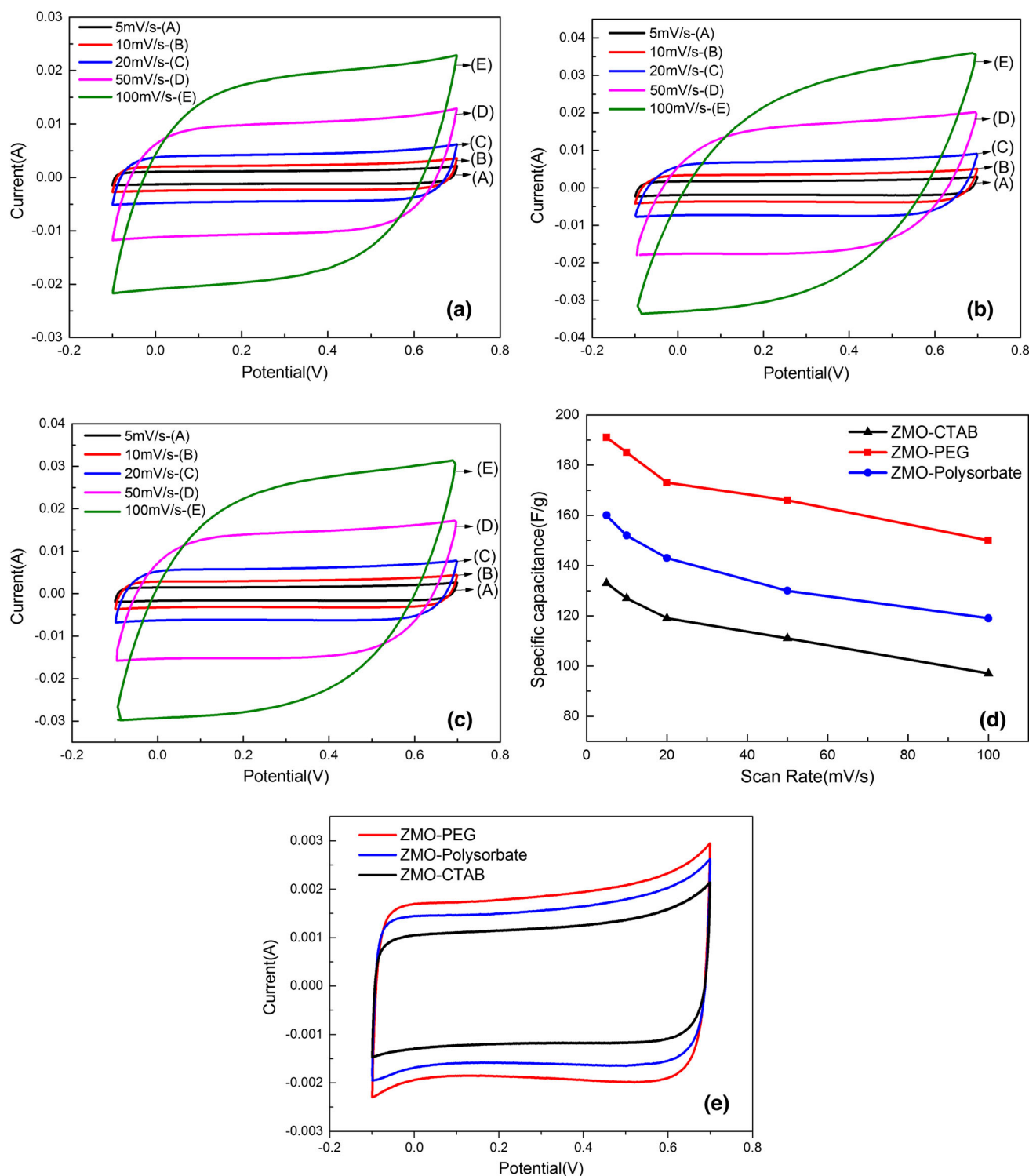


Fig. 4. CV curves for (a) ZMO-CTAB, (b) ZMO-PEG, and (c) ZMO-Polysorbate samples obtained at various scan rates. (d) Specific capacitance of ZMO samples at various scan rates. (e) CV curves of ZMO samples at scan rate of  $5 \text{ mV s}^{-1}$ .

exhibited a fast and reversible reaction, showing ideal electrical capacitive behavior for active capacitor materials. All the CV curves clearly show basically rectangular shape with symmetric nature, with no redox peak observed. It is suggested that

the ZMO samples exhibit faster charge propagation and easy ion transport due to electric double-layer capacitance (ELDC) behavior.<sup>24</sup>

The specific capacitance values calculated for the ZMO-CTAB, ZMO-PEG, and ZMO-Polysorbate

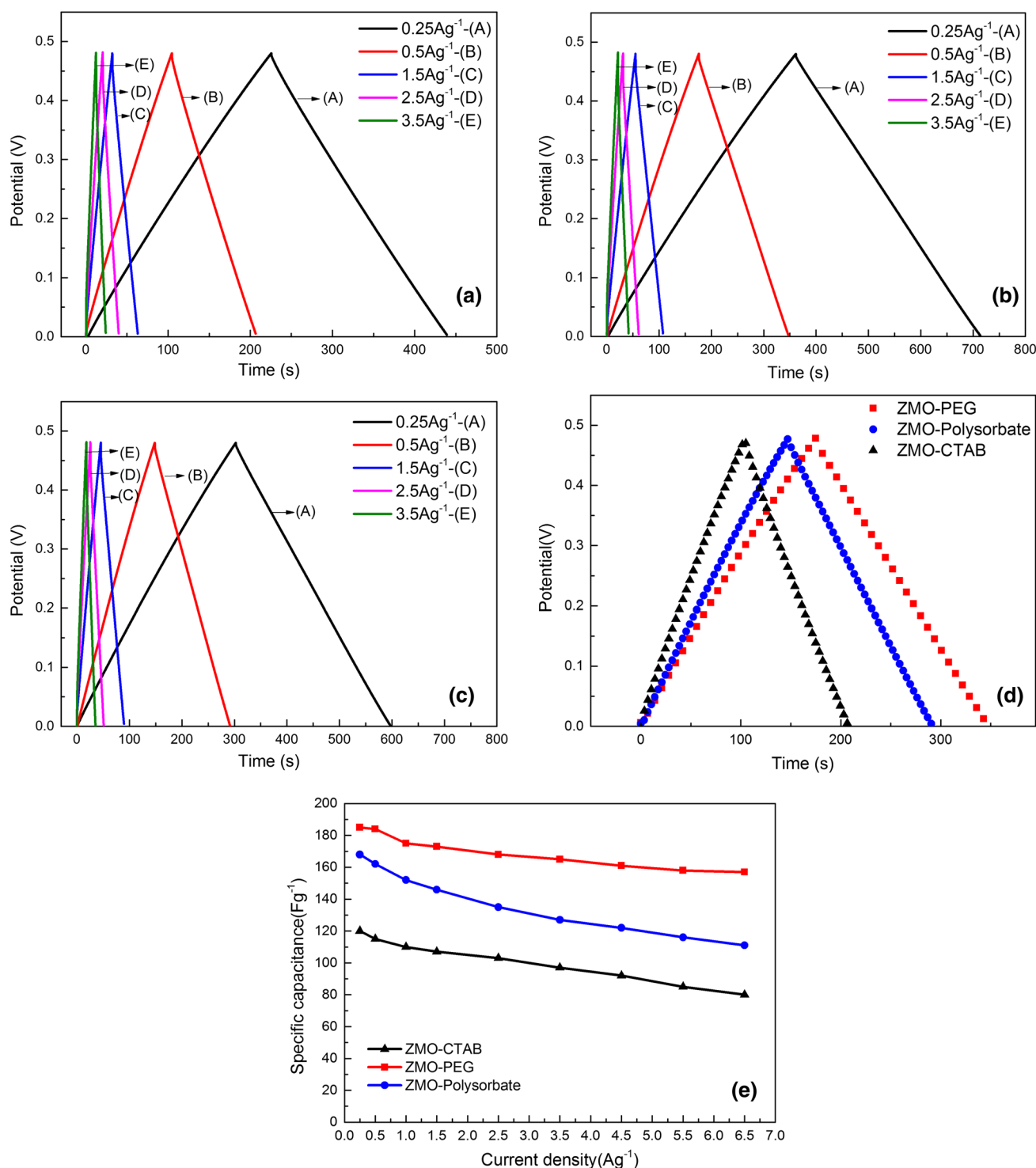


Fig. 5. Galvanostatic charge-discharge curves of (a) ZMO-CTAB, (b) ZMO-PEG, and (c) ZMO-Polysorbate samples at different current densities. (d) Galvanostatic charge-discharge curves of ZMO samples at current density of 2  $\text{A g}^{-1}$ . (e) Specific capacitance of ZMO samples at various current densities.

samples are plotted versus scan rate in Fig. 4d. These curves reveal that the specific capacitance of all the samples gradually decreased with increase of the scan rate. This indicates that, at higher scan rates, the electrodes possessed lower energy storage

efficiency due to the lower diffusion rate of electrolyte into each electrode material. The estimated highest specific capacitance of ZMO-CTAB, ZMO-PEG, and ZMO-Polysorbate was 133  $\text{F g}^{-1}$ , 191  $\text{F g}^{-1}$ , and 160  $\text{F g}^{-1}$ , respectively, at scan rate

of  $5 \text{ mV s}^{-1}$ . In addition, the ZMO-CTAB, ZMO-PEG, and ZMO-Polysorbate samples showed capacitance retention of 71%, 79%, and 75% when the scan rate was increased from  $5 \text{ mV s}^{-1}$  to  $100 \text{ mV s}^{-1}$ . Moreover, the specific capacitance of the ZMO-PEG electrode was clearly superior to those made from ZMO-CTAB and ZMO-Polysorbate at given scan rate. Obviously, the choice of the surfactant not only influenced the morphology and structure, but also affected the specific capacitance of the ZMO samples. Compared with the ZMO-CTAB and ZMO-Polysorbate samples, the superior specific capacitance of ZMO-PEG can mainly be attributed to its loose and porous microsphere architecture. It is speculated that the larger surface area and pore structure create more channels for electrolyte movement at the electrode–electrolyte interface.

To further investigate the advantages of the ZMO samples, CV curves for the ZMO-CTAB, ZMO-PEG, and ZMO-Polysorbate samples were recorded at scan rate of  $5 \text{ mV s}^{-1}$  in the potential window of  $-0.1 \text{ V}$  to  $0.7 \text{ V}$  (Fig. 4e), revealing the poorest specific capacitance for ZMO-CTAB, with the smallest CV loop area. At the same time, the CV loop area of ZMO-PEG and ZMO-Polysorbate was relatively large, reflecting their relatively higher capacitance and better electrochemical reaction.

The charge transfer rate and  $\text{Na}^+$  diffusion rate have a direct effect on the rate capability. The reaction mechanism of  $\text{ZnMn}_2\text{O}_4$  as the negative electrode material can be expressed by the following equations:

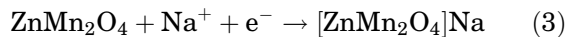
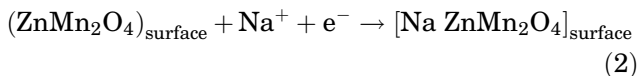


Figure 5a, b, and c present the GCD curves for the ZMO-CTAB, ZMO-PEG and ZMO-Polysorbate samples obtained at different current densities from  $0.25 \text{ A g}^{-1}$  to  $3.5 \text{ A g}^{-1}$  in the potential window of  $0 \text{ V}$  to  $0.48 \text{ V}$ . All the curves clearly display a nearly linear isosceles triangle, and the charge curves are symmetric to the discharge curves, indicating supercapacitive behavior with rapid  $I$ – $V$  response. The GCD curves for the ZMO-CTAB, ZMO-PEG, and ZMO-Polysorbate samples obtained at current density of  $2 \text{ A g}^{-1}$  are illustrated in Fig. 5d. The clear symmetry of the GCD curves during the charge and discharge processes confirms the perfect supercapacitive property.

Figure 5e shows the specific capacitance versus the current density for the ZMO-CTAB, ZMO-PEG, and ZMO-Polysorbate samples, showing a decrease with increase of the current density for all samples, which may be due to the decrease of the internal resistance of  $\text{ZnMn}_2\text{O}_4$  leading to a decrease of the total capacitance. Moreover, ZMO-PEG was stable relative to the other two samples. The

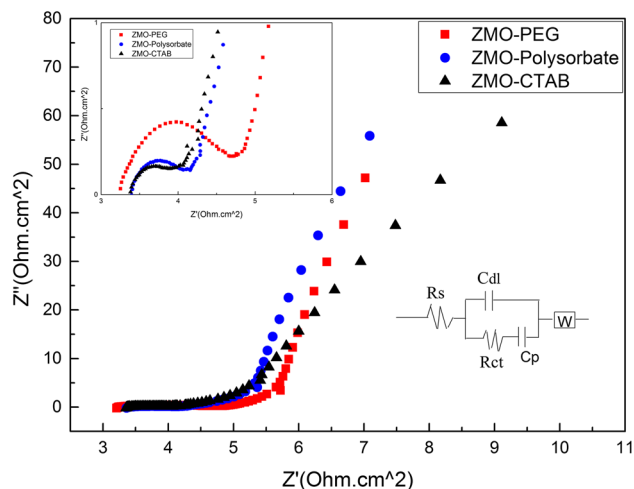


Fig. 6. Nyquist plots of ZMO samples and equivalent circuit model.

reducing trend of the capacitance with increase of the current density was relatively moderate. In addition, the specific capacitance of the ZMO-PEG electrode at given current density was clearly higher than for the ZMO-CTAB or ZMO-Polysorbate electrode.

To evaluate the electrochemical properties of the resulting supercapacitors, the electrodes were investigated using EIS. Figure 6 shows Nyquist plots and the equivalent circuit for the ZMO-CTAB, ZMO-PEG, and ZMO-Polysorbate samples. The Nyquist plots of the impedance spectra are clearly similar in shape, indicating the existence of equivalent diffusion ability for the ZMO samples. The Nyquist plots included a semicircle in the high-frequency region and similar straight lines in the low-frequency region. The equivalent circuit includes the solution resistance  $R_s$ , charge-transfer resistance  $R_{ct}$ , double-layer capacitance  $C_d$ , pseudo-capacitance  $C_p$ , and Warburg impedance  $W$  (Fig. 6, inset). The inset of Fig. 6 shows the spectra in the high-frequency region, where the diameter of the semicircle indicates the charge-transfer resistance ( $R_{ct}$ ), while the slope of the Nyquist plots represents the resistance ( $Z_w$ ) to ion diffusion in the electrolyte. The  $R_{ct}$  value for the ZMO-CTAB, ZMO-PEG, and ZMO-Polysorbate samples was found to be  $0.61 \Omega$ ,  $1.45 \Omega$ , and  $0.72 \Omega$  (Fig. 6, inset), respectively, revealing better electrical conductivity. These findings reveal that the equivalent series resistance is small, and such ZMO materials would be suitable for use as electrodes for supercapacitors with good frequency response characteristics.

Also, the  $Z_w$  value is larger for the ZMO-CTAB sample compared with the ZMO-PEG or ZMO-Polysorbate sample, demonstrating the lowest impedance caused by ion diffusion within the electroactive materials. In addition, the  $x$ -intercept of the semicircle with the real axis yields the internal resistance ( $R_s$ ), including the ionic resistance of the electrolyte, the intrinsic resistance of the electrode



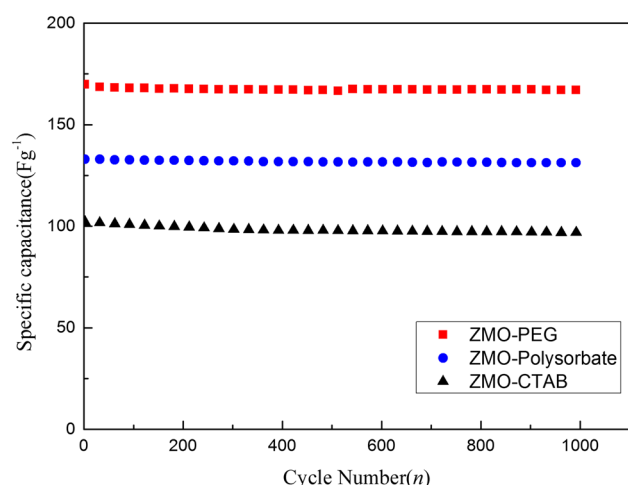


Fig. 7. Cycling performance of ZMO samples at current density of  $2.5 \text{ A g}^{-1}$ .

materials, and the contact resistance at the electrode–electrolyte interface. It can be seen that the  $R_s$  value for the ZMO-CTAB, ZMO-PEG, and ZMO-Polysorbate samples was about  $3.39 \Omega$ ,  $3.24 \Omega$ , and  $3.36 \Omega$ , respectively. The  $R_s$  value for the ZMO-PEG sample is the lowest, suggesting that this sample exhibits rapid electron transfer with optimal conductivity, as well as excellent specific capacitance.

Cycle stability testing with the ZMO-CTAB, ZMO-PEG, and ZMO-Polysorbate samples as electrode material was carried out at current density of  $2.5 \text{ A g}^{-1}$  for 1000 cycles, as shown in Fig. 7. Figure 7 shows a plot of the specific capacitance as a function of cycle number; the specific capacitance of ZMO-CTAB, ZMO-PEG, and ZMO-Polysorbate in the initial cycle was  $103 \text{ F g}^{-1}$ ,  $169 \text{ F g}^{-1}$ , and  $133 \text{ F g}^{-1}$ , respectively, at current density of  $2.5 \text{ A g}^{-1}$ . After 1000 charge–discharge cycles, the specific capacitance of the ZMO-CTAB, ZMO-PEG, and ZMO-Polysorbate samples remained at about  $98 \text{ F g}^{-1}$ ,  $166 \text{ F g}^{-1}$ , and  $130 \text{ F g}^{-1}$ , representing about 93.8%, 98.4%, and 97.7% of the initial value, respectively. This demonstrates that the  $\text{ZnMn}_2\text{O}_4$  nanopowders possessed excellent electrochemical stability and good reversibility. It can be concluded that the choice of surfactant had a strong influence on the specific capacitance of the samples, with the specific capacitance and cycling performance of ZMO-PEG being found to be superior to those of ZMO-CTAB and ZMO-Polysorbate. Such better electrochemical performance of ZMO-PEG can be ascribed to a synergistic effect.  $\text{ZnMn}_2\text{O}_4$  is very promising as a supercapacitor material.

## CONCLUSIONS

ZMO-CTAB, ZMO-PEG, and ZMO-Polysorbate for use as the negative electrode in supercapacitors were successfully synthesized via a facile hydrothermal method. The three types of  $\text{ZnMn}_2\text{O}_4$

nanopowder exhibited single-phase spinel tetragonal structure, with honeycomb, spinel microsphere, and flower-cluster morphology, respectively. They exhibited good crystallinity and electrochemical properties. The CV curves were close to rectangular in shape, with no significant redox peak. The estimated highest specific capacitance of ZMO-CTAB, ZMO-PEG, and ZMO-Polysorbate was  $133 \text{ F g}^{-1}$ ,  $191 \text{ F g}^{-1}$ , and  $160 \text{ F g}^{-1}$  at scan rate of  $5 \text{ mV s}^{-1}$ . The  $R_s$  value for ZMO-PEG was the lowest among the three samples. The materials retained approximately 93.8%, 98.8%, and 98.4% of the initial capacitance after 1000 charge–discharge cycles at current density of  $2.5 \text{ A g}^{-1}$ . The electrochemical behavior of the ZMO-PEG electrode was superior to those formed from ZMO-CTAB and ZMO-Polysorbate. Compared with traditional electrode materials such as activated carbon, with operating voltage generally greater than 1 V and theoretical specific capacity generally around  $100 \text{ F g}^{-1}$ ,<sup>25,26</sup>  $\text{ZnMn}_2\text{O}_4$  offers lower operating voltage (0.8 V) and better electrical capacitance (near  $200 \text{ F g}^{-1}$ ). For cobalt-based metal-oxide electrode materials, the specific capacitance can range from  $689 \text{ F g}^{-1}$  to  $2468 \text{ F g}^{-1}$ .<sup>27,28</sup> The electrical capacity of these  $\text{ZnMn}_2\text{O}_4$  materials is not high and remains far from its theoretical value. However, the low internal resistance and fairly stable charge–discharge cycling performance indicate promise as supercapacitor electrode materials.

## ACKNOWLEDGEMENT

This work was supported by the National Natural Science Foundation of China (No. 51261015) and the Natural Science Foundation of Gansu Province, China (No. 1308RJZA238).

## REFERENCES

- Y. Li, L.-B. Kong, M.-C. Liu, W.-B. Zhang, and L. Kang, *Mater. Lett.* 186, 289 (2017).
- H. Wu, G. Wu, Y. Ren, X. Li, and L. Wang, *Chemistry* 22, 8864 (2016).
- G.R. Xu, X.P. Min, Q.L. Chen, Y. Wen, A.P. Tang, and H.S. Song, *J. Alloys Compd.* 691, 1018 (2017).
- T. Zhang, L.-B. Kong, M.-C. Liu, Y.-H. Dai, K. Yan, B. Hu, Y.-C. Luo, and L. Kang, *Mater. Des.* 112, 88 (2016).
- W. Ma, S. Chen, S. Yang, W. Chen, Y. Cheng, Y. Guo, S. Peng, S. Ramakrishna, and M. Zhu, *J. Power Sources* 306, 481 (2016).
- M. Huang, Y. Zhang, F. Li, L. Zhang, Z. Wen, and Q. Liu, *J. Power Sources* 252, 98 (2014).
- H. Wu, G. Wu, Y. Ren, L. Yang, L. Wang, and X. Li, *J. Mater. Chem. C* 3, 7677 (2015).
- G.H. Yue, Y.C. Zhao, C.G. Wang, X.X. Zhang, X.Q. Zhang, and Q.S. Xie, *Electrochim. Acta* 152, 315 (2015).
- H. Wu, G. Wu, and L. Wang, *Powder Technol.* 269, 443 (2015).
- T. Zhang, Y. Gao, H. Yue, H. Qiu, Z. Guo, Y. Wei, C. Wang, G. Chen, and D. Zhang, *Electrochim. Acta* 198, 84 (2016).
- L.X. Zhang, Y.L. Wang, H.F. Jiu, H.Y. Qiu, and H.Y. Wang, *Ceram. Int.* 41, 9655 (2015).
- D. Cai, D. Wang, H. Huang, X. Duan, B. Liu, L. Wang, Y. Liu, Q. Li, and T. Wang, *J. Mater. Chem. A* 3, 11430 (2015).
- L. Xiao, Y. Yang, J. Yin, Q. Li, and L. Zhang, *J. Power Sources* 194, 1089 (2009).



14. X.X. Lin, Y.F. Zhu, and W.Z. Shen, *J. Phys. Chem. C* 113, 1812 (2009).
15. Z. Wang, J. Zhang, Y. Yang, and Ling, *J. Wuhan Univ. Technol. (Mater. Sci. Edn.)* 30, 1159 (2015).
16. P. Li, J. Liu, Y. Liu, Y. Wang, Z. Li, W. Wu, Y. Wang, L. Yin, H. Xie, and M. Wu, *Electrochim. Acta* 180, 164 (2015).
17. W. Dang, F. Wang, Y. Ding, C. Feng, and Z. Guo, *J. Alloys Compd.* 690, 72 (2017).
18. F.M. Courtel, Y. Abu-Lebdeh, and I.J. Davidson, *Electrochim. Acta* 71, 123 (2012).
19. F. Courtel, H. Duncan, Y. Abulebdeh, and I. Davidson, *J. Mater. Chem.* 21, 10206 (2011).
20. L. Zhao, X. Li, and J. Zhao, *Appl. Surf. Sci.* 268, 274 (2013).
21. A. Sahoo and Y. Sharma, *Mater. Chem. Phys.* 149, 721 (2015).
22. R. Gherbi, Y. Bessekhoud, and M. Trari, *J. Phys. Chem. Solids* 89, 69(9) (2016).
23. B. Ameri, S.S.H. Davarani, H.R. Moazami, and H. Darjazi, *J. Alloys Compd.* 720, 5 (2017).
24. N. Guo, X.Q. Wei, X.L. Deng, and X.J. Xu, *Appl. Surf. Sci.* 356, 1127 (2015).
25. L. Demarconnay, E. Raymundo-Piñero, and F. Béguin, *Electrochem. Commun.* 1275, 12 (2010).
26. C. Portet, P.L. Taberna, and P. Simon, *Electrochim. Acta* 4174, 50 (2005).
27. G. Zhou, J. Zhu, and Y. Chen, *Electrochim. Acta* 450, 123 (2014).
28. K. Qiu, Y. Lu, and D. Zhang, *Mesoporous Nano Energy* 687, 11 (2015).